Lanthanide-Based Probes for Imaging Detection of Enzyme Activities by NIR Luminescence, T1- and ParaCEST MRI

Rémy Jouclas, Sophie Laine, Svetlana V. Eliseeva, Jérémie Mandel, Frédéric Szeremeta, Pascal Retailleau, Jiefang He, Jean-françois Gallard, Agnès Pallier, Célia S. Bonnet, et al.

How to cite: *Angew. Chem. Int. Ed.* **2024**, *63*, e202317728
doi.org/10.1002/anie.202317728

Mutimodal Imaging

Lanthanide-Based Probes for Imaging Detection of Enzyme Activities by NIR Luminescence, T1- and ParaCEST MRI

Rémy Jouclas, Sophie Laine, Svetlana V. Eliseeva, Jérémie Mandel, Frédéric Szeremeta, Pascal Retailleau, Jiefang He, Jean-François Gallard, Agnès Pallier, Célia S. Bonnet, Stéphane Petoud, Philippe Durand,* and Éva Tóth**

Abstract: Applying a single molecular probe to monitor enzymatic activities in multiple, complementary imaging modalities is highly desirable to ascertain detection and to avoid the complexity associated with the use of agents of different chemical entities. We demonstrate here the versatility of lanthanide (Ln^{3+}) complexes with respect to their optical and magnetic properties and their potential for enzymatic detection in NIR luminescence, CEST and T1 MR imaging, controlled by the nature of the Ln^{3+} ion, while using a unique chelator. Based on X-ray structural, photophysical, and solution NMR investigations of a family of Ln^{3+} DO3A-pyridine model complexes, we could rationalize the luminescence (Eu^{3+}, Yb^{3+}), CEST (Yb^{3+}) and relaxation (Gd^{3+}) properties and their variations between carbamate and amine derivatives. This allowed the design of $\boldsymbol{LnL^{5}_{Gal}}$ probes which undergo enzyme-mediated changes detectable in NIR luminescence, CEST and T1-weighted MRI, respectively governed by variations in their absorption energy, in their exchanging proton pool and in their size, thus relaxation efficacy. We demonstrate that these properties can be exploited for the visualization of β-galactosidase activity in phantom samples by different imaging modalities: NIR optical imaging, CEST and T1-weighted MRI.

[*] Dr. S. Laine, Dr. S. V. Eliseeva, Dr. F. Szeremeta, A. Pallier, Dr. C. S. Bonnet, Prof. Dr. S. Petoud, Dr. É. Tóth
Centre de Biophysique Moléculaire, CNRS UPR 4301, Université d'Orléans, rue Charles Sadron, 45071 Orléans, France
E-mail: stephane.petoud@inserm.fr
eva.jakabtoth@cnrs-orleans.fr

Dr. R. Jouclas, Dr. J. Mandel, Dr. P. Retailleau, Dr. J. He, J.-F. Gallard, Dr. P. Durand
Université Paris-Saclay, CNRS, Institut de Chimie des Substances Naturelles, UPR 2301, 91198 Gif-sur-Yvette, France
E-mail: philippe.durand@cnrs.fr

Introduction

Molecular imaging of enzymes has a strong interest in medicine and in biomedical research. A large number of pathologies are associated with enzymatic imbalance, and more than one-fourth of available drugs today target enzymes.[1] Detecting proteins in a living organism is challenging due to their very low concentration. In the case of enzymes, this limitation can be overcome by harnessing their catalytic activity. Imaging then relies on the monitoring of enzyme-catalyzed production of detectable chemical species, enabling a real-time knowledge of the amount of working enzymes in a specific biological medium.[2–3] While this activity can be assessed from biological sampling with *in vitro* assays, *in vivo* or *in cellulo* detection is preferable, since the activity may depend on enzyme localization and environmental factors. Responsive probes have been created for real-time and non-destructive visualization of enzyme activities in cells or in deep tissues by optical, magnetic resonance imaging (MRI) and nuclear imaging techniques.[2–6] Each imaging modality possesses specific advantages and limitations; their combination in multimodal approaches allowing cellular- and organism-level visualization has become a critical asset to overcome the pitfalls of the individual techniques. For such applications, a single probe generating signals in all modalities is preferred. This approach removes the complexity of using various agents with different chemical compositions, solubility, toxicity, biodistribution, pharmacokinetics, etc.[7–9]

Lanthanide (Ln^{3+}) complexes offer unique and versatile luminescence and magnetic properties. Several Ln^{3+} possess complementary advantages[10–13] over luminescence properties of organic fluorophores and semi-conductor nanocrystals: (i) sharp emission bands, the barycenter of which does not shift upon changes of experimental conditions, allowing for spectral discrimination. (ii) Several Ln^{3+} emit in the near-infrared (NIR) I and II domains. The detection in this spectral domain allows the removal of the unwanted contribution of the native fluorescence of biological material (autofluorescence), simplifying experiments and preventing ambiguity in the interpretation of the results. (iii) Most of Ln^{3+} complexes possess strong resistance to photobleaching for long or repeated experiments. The key requirement to generate the luminescence of Ln^{3+} ions is their sensitization with appropriate chromophoric group(s).

In respect to magnetic properties, Ln^{3+} complexes can generate contrast detectable in classical, relaxation-based T1-weighted MRI (Ln^{3+} = Gd), or in CEST MRI based on proton exchange between the probe and bulk water (CEST = Chemical Exchange Saturation Transfer; all paramagnetic Ln^{3+} except Gd^{3+}), with tunable properties.[14–15] Given the very similar coordination chemistry of Ln^{3+} ions, a single ligand can be used for the complexation of various luminescent and MRI-active cations for multimodal detection; these complexes formed with the different Ln^{3+} ions will have identical biodistribution. Several examples of Ln^{3+}-based bimodal MRI/optical probes have been described,[16–20] but very few are dedicated to the detection of enzyme activity.[21–24]

We have previously reported that the carbamate-to-amine conversion in DO3A-pyridine-based Ln^{3+} complexes (LnL^6, Scheme 1)[25] induces remarkable variations in the luminescence intensity and in the CEST signals for Tb^{3+} and Yb^{3+} complexes, and in the relaxivity of the Gd^{3+} analogue. The use of a self-immolative benzyl carbamate[26–31] can render such systems responsive to molecular events such as enzymatic cleavage.

Here, we describe the first demonstration that the enzyme-mediated carbamate-to-amine conversion in Ln^{3+}-DO3A-pyridine derivatives makes the detection of enzymatic activities possible in complementary imaging modalities, including NIR luminescence, T1 and CEST MRI. First, the comparison of three series of model Ln^{3+} complexes, ***LnL^n*** and ***LnL$^n_{NH2}$*** (n = 3 to 5 corresponds to the position of the carbamate or the amine on the pyridine; Ln^{3+} = Gd, Yb, Eu; Scheme 1) allowed us to identify the optimized ligand structure with combined detection capabilities in NIR optical, T1 and CEST MR imaging. X-ray crystallography on single crystals of all Yb^{3+} analogues and solution NMR studies were used to establish structure–activity relationships. The promising luminescence, CEST and relaxivity properties obtained with ***LnL^5***/***LnL$^5_{NH2}$*** complexes led us to design and synthesize the enzyme-responsive probes ***LnL$^5_{Gal}$*** for the monitoring of β-galactosidase activity. Upregulation of β-galactosidase is often correlated with the occurrence of cancers and cell senescence; thus, *in vivo* detection and localization of β-galactosidase activities can become an essential tool for cancer diagnosis and treatment monitoring.[32–33] This biological interest has led to the development of responsive probes for *in cellulo* and *in vivo* detection.[5,34–39] We demonstrate here that ***LnL$^5_{Gal}$*** allows successful imaging of β-galactosidase activity by NIR luminescence (***YbL$^5_{Gal}$***), T1-weighted (***GdL$^5_{Gal}$***) and CEST MRI (***YbL$^5_{Gal}$***).

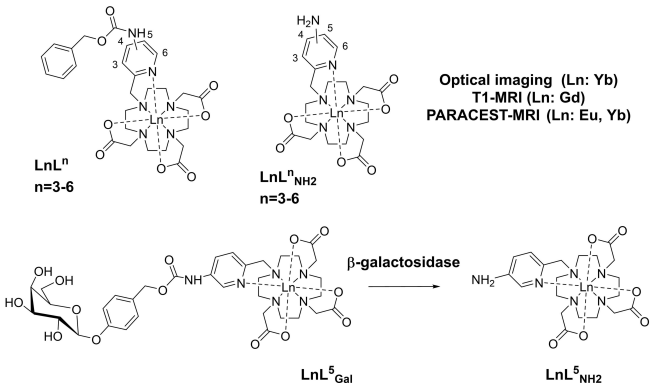

Scheme 1. Chemical structures of model complexes ***LnL^n***/***LnL$^n_{NH2}$*** and of the β-galactosidase-responsive ***LnL$^5_{Gal}$*** probe. *n* corresponds to the position on the pyridine; n = 6 : ref. [25], n = 3–5: this work.

Results and Discussion

Ligands $\mathbf{H_3L^n}$ (n = 3–5) and their corresponding $\mathbf{LnL^n}$ complexes were synthesized by adapting previously reported procedures.[25] Hydrogenolysis of $\mathbf{LnL^n}$ complexes led to the formation of the corresponding $\mathbf{LnL^n_{NH2}}$ chelates. $\mathbf{LnL^5_{Gal}}$ complexes carrying an enzyme-sensitive galactosylated benzyl carbamate were obtained by adapting the procedure used for $\mathbf{LnL^5}$. All synthetic details are given in the Supporting Information.

Investigation of Model Complexes

X-ray solid-state structures have been determined for $\mathbf{YbL^{3-5}}$ and $\mathbf{YbL^{3-5}_{NH2}}$ (Figure 1 and Table 1; see Supporting Information for crystallographic data and their discussion). All complexes are eight-coordinate and adopt a twisted square antiprismatic geometry. This situation contrasts with the nine-coordination found in $\mathbf{GdL^6}$ and $\mathbf{EuL^6}$.[25,40] $\mathbf{L^{3-5}}$ and $\mathbf{L^{3-5}_{NH2}}$ are coordinated to the Yb^{3+} in an octadentate fashion (four macrocyclic nitrogen atoms, one pyridine nitrogen and three carboxylate oxygens). The O–Ln–O/N ("opening") angles between the trans annular carboxylate oxygen and pyridine nitrogen atoms located in the O3N plane (ω, ω′ = 122–127° (Table 1, Figure S119) are fully

Table 1: Selected distances and angles measured from the X-ray solid-state structures (XR) of ***YbL$^{3-5}$*** and ***YbL$^{3-5}_{NH2}$***.

	YbL^3	***YbL^4***	***YbL^5***	***YbL$^3_{NH2}$***	***YbL$^4_{NH2}$***	***YbL$^5_{NH2}$***
d(Yb–Q_{N4})[a] (Å)	1.464	1.458	1.443	1.453	1.444	1.469
d(Yb–Q_{O3N})[b] (Å)	1.075	1.092	1.096	1.102	1.071	1.089
d(N3–N27) (Å)	2.732(6)	2.766(8)	2.751(7)	2.741(3)	2.712(2)	2.780(2)
ω : Λ(O24–Yb–O16)[c] (°)	122.5(2)	124.9(2)	124.8(1)	124.22(6)	125.62(4)	123.8(4)
ω': Λ(O20–Yb–N27)[c] (°)	126.7(1)	122.3(2)	121.5(1)	122.19(6)	123.98(5)	124.1(4)
Γ(Yb–N3–C25–C26)[d] (°)	±151.3(5)	±154.1(6)	±163.6(4)	±159.4(2)	±170.02(15)	±145.1(1)

[a] centroids of N4-planes (PN4). [b] centroids of O3N-planes (PO3N). [c] opening angle, [d] torsion angle.

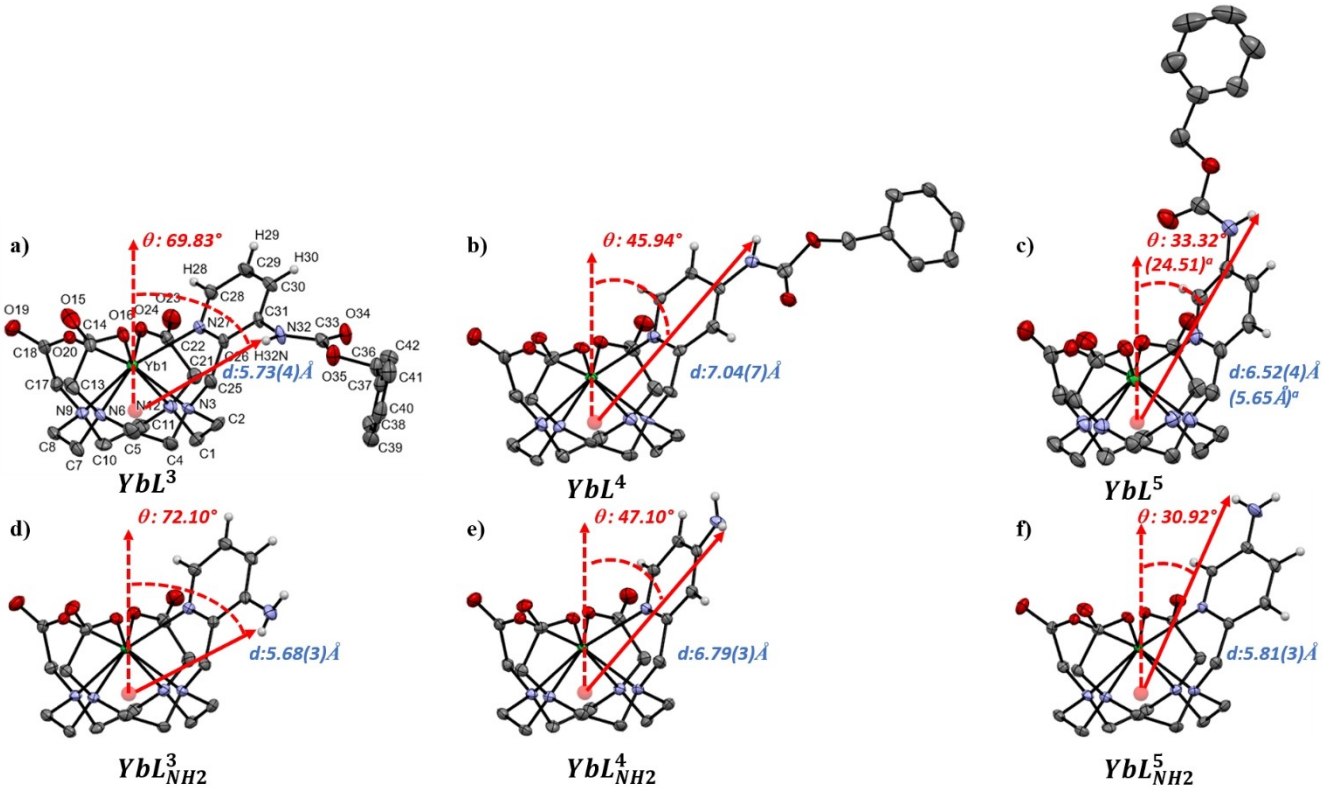

Figure 1. ORTEP-III plots[42] of enantiomers Δ(δδδδ) in the unit cell of the complexes a) ***YbL***^{3}, b) ***YbL***^{4}, c) ***YbL***^{5}, d) ***YbL***$^3_{NH2}$, e) ***YbL***$^4_{NH2}$ and f) ***YbL***$^5_{NH2}$ (generated from CIF files using the Mercury software[43]). Ellipsoids are drawn at the 50% probability level and, for clarity, H atoms of the macrocycle and solvent molecules are not shown. The side-on views of all the complexes are given with the same orientation. Dashed red arrow: axis passing through the N_4 macrocycle centroid (orange sphere) and Yb^{3+}, solid red arrow: vector linking N_4 macrocycle centroid to the carbamate or amine protons; *θ*: angle between these two axes; *d*: distance from the Yb^{3+} to the amine or carbamate proton. [a] calculated for the assumed solution structure of ***YbL***$^{5'}$.

consistent with a structure where Ln^{3+} is not coordinated by any water molecule, for which a limiting angle value of ≈135° was proposed.[41] In contrast to **LnL**^{6} analogues, crystal structures of **YbL**$^{3-5}$ demonstrate that the carbamate moiety adopts a non-coordinating position.

Despite their high degree of similarity, the crystal structures of **YbL**$^{3-5}$ and **YbL**$^{3-5}_{NH2}$ do show variations with changes of the substituent position on the pyridine ring. More specifically, the distance and the position of the carbamate or amine protons with respect to Yb^{3+} are affected, which will be reflected in the CEST properties. The dihedral angle $\Gamma_{Yb-N(3)-C(25)-C(26)}$ involving the methyl pyridine arm varies in the ranges of 42.51°–48.95° within the **YbL**$^{3-5}$ and 41.4°–50.5° within the **YbL**$^{3-5}_{NH2}$ series, while the distance between the pyridine N27 and the macrocycle N3 remains similar (Table 1, Figure S120). These results indicate varying pyridine ring orientations, with the N(27)–C(30) axis of the pyridine tilted in respect to the Yb–N(27) axis from 6.4° to 16.5° within the **YbL**$^{3-5}$ series and from 4.58° to 25.74° within the **YbL**$^{3-5}_{NH2}$ series (Tables S16, S17, Figures S120–123). Importantly, for **YbL**^{5}, the N–CO carbamate bond adopts an anti-conformation in respect to the N–H bond (Figure 1c), stabilized by an intermolecular hydrogen bond (Figure S124) which is likely disrupted in solution, leading to a different relative orientation of the carbamate and of the pyridine. A model of this structure in solution (**YbL**$^{5'}$) was built from the XR data of **YbL**^{5} using CCP4 and Coot softwares and yielded a considerably shorter Yb-carbamate proton (H_{32}) distance, 5.64 Å (vs. 6.52(5) Å in the solid structure). This shorter distance in solution is important for the CEST effect (see below).

In order to assess the potential of Ln^{3+}-DO3A-pyridine chelates for enzymatic detection by NIR luminescence, photophysical data were collected for 100 μM solutions of ***LnL***$^{3-5}$ and ***LnL***$^{3-5}_{NH2}$ (Ln^{3+} = Eu, Yb) complexes in HEPES buffer (pH = 7.4) at room temperature. Absorption spectra (Figures 2a–c, S127 a-c) are independent of the nature of the Ln^{3+}. ***LnL***^{3}/***LnL***^{5} and ***LnL***$^3_{NH2}$/***LnL***$^5_{NH2}$ display two broad bands in the UV range, centered at 237 nm, 272 nm/241 nm, 288 nm, and 237 nm, 299 nm/242 nm, 306 nm, respectively. In contrast, only one broad band centered at 250 nm and 254 nm is observed for ***LnL***^{4} and ***LnL***$^4_{NH2}$, respectively. It is important to note the redshift in the low energy absorption maxima from ***LnL***$^{3-5}$ to the corresponding ***LnL***$^{3-5}_{NH2}$ complexes, which increases in the order ***LnL***^{4}/***LnL***$^4_{NH2}$ (4 nm) < ***LnL***^{5}/***LnL***$^5_{NH2}$ (18 nm) < ***LnL***^{3}/***LnL***$^3_{NH2}$ (27 nm). A larger energy difference between absorption bands for complexes before and after the enzymatic cleavage is advantageous to create responsive probes, as it

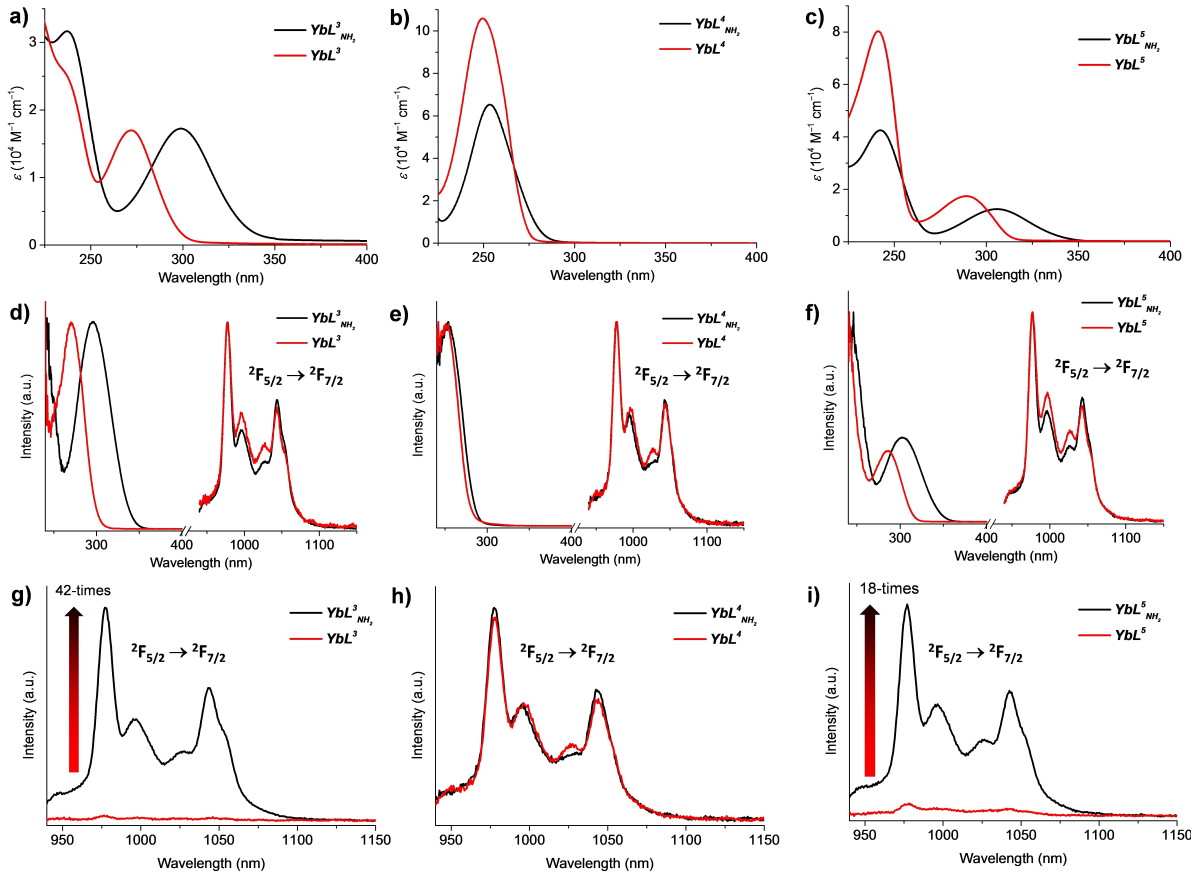

Figure 2. Photophysical data for 100 μM solutions of $\boldsymbol{YbL^n}$ (red traces) and $\boldsymbol{YbL^n_{NH2}}$ (black traces) in HEPES buffer (n = 3–5, pH 7.4, room temperature). a)–c) Absorption spectra. d)–f) Corrected and normalized (left) excitation (λ_{em} = 978 nm) and (right) emission (λ_{ex} = 260–310 nm) spectra. g)–i) Comparison of the emission spectra under excitation at g) 310 nm; h) 260 nm; i) 320 nm.

will facilitate the optical detection. For example, only $\boldsymbol{LnL^3_{NH2}}$ and $\boldsymbol{LnL^5_{NH2}}$ complexes, but not $\boldsymbol{LnL^3}$ and $\boldsymbol{LnL^5}$, exhibit absorption at 310 and 320 nm, respectively, allowing selective excitation at those wavelengths. The change of absorption is, however, not a unique parameter to be considered when designing luminescent Ln^{3+}-based responsive probes; Ln^{3+} sensitization efficiencies provided by organic chromophores can also be modified in response to a stimulus.[44]

Excitation spectra recorded upon monitoring the main Eu^{3+} and Yb^{3+} transitions at 615 and 980 nm, respectively, match the shapes of the absorption spectra, indicating that sensitization of both Ln^{3+} ions occurs through the electronic states localized on the chromophoric ligands (Figures 2d–f and S127d–f). Upon excitation into the respective ligand-centered absorption bands in the range 260–310 nm, Eu^{3+} and Yb^{3+} complexes exhibit their characteristic narrow emission bands in the visible (Eu^{3+}) or in the NIR (Yb^{3+}) range. Relative ratios of different f-f transitions and crystal-field splitting of the bands in the emission spectra of the corresponding $\boldsymbol{LnL^{3-5}}$ and $\boldsymbol{LnL^{3-5}_{NH2}}$ remain almost completely unchanged, confirming similar Ln^{3+} coordination environments.

Ln^{3+}-centered quantum yields $\boldsymbol{Q^L_{Ln}}$ (Table S21) represent the ability of the chromophoric ligand to transfer energy to the luminescent Ln^{3+} which is correlated to the amount of emitted signal. Measured $\boldsymbol{Q^L_{Ln}}$ values are 13–85 times lower for $\boldsymbol{EuL^{3-5}_{NH2}}$ than for the corresponding $\boldsymbol{EuL^{3-5}}$, which is likely due to a more pronounced quenching of Eu^{3+} emission through a photo-induced electron transfer (PET) in $\boldsymbol{EuL^{3-5}_{NH2}}$.[45–46] The highest $\boldsymbol{Q^L_{Eu}}$ values are observed for $\boldsymbol{EuL^4}$ (1.84 ± 0.01 %) and $\boldsymbol{EuL^4_{NH2}}$ (0.08 ± 0.01 %). For Yb^{3+}, $\boldsymbol{Q^L_{Yb}}$ does not vary significantly between $\boldsymbol{YbL^{3-5}}$ (0.036–0.063 %) and $\boldsymbol{YbL^{3-5}_{NH2}}$ complexes (0.036–0.041 %). Experimental luminescence decay signals, recorded upon monitoring the emission of Eu^{3+} at 615 nm or of Yb^{3+} at 978 nm, are i) monoexponential for $\boldsymbol{LnL^{3-5}}$, reflecting the existence of Ln^{3+} emitting species in a single coordination environment, ii) biexponential for $\boldsymbol{LnL^{3-5}_{NH2}}$. The latter result suggests the presence of Ln^{3+} in two different coordination environments or differently affected by the quenching processes. For both Eu^{3+} and Yb^{3+} complexes, luminescence lifetimes (τ_{obs}) are shorter for $\boldsymbol{LnL^{3-5}}$ compared to $\boldsymbol{LnL^{3-5}_{NH2}}$. Luminescence decays were also recorded in D_2O solutions to estimate the Ln^{3+} hydration number, q, using phenomenological equations (Table S21).[47–48] One inner sphere water molecule was measured for $\boldsymbol{EuL^{3,4}}$ and $\boldsymbol{EuL^{3,4}_{NH2}}$. For $\boldsymbol{EuL^5}$ and $\boldsymbol{EuL^5_{NH2}}$, the hydration number was found to be 2. It should be noted, however, that the use of phenomenological equations is unreliable if several quenching mecha-

nisms are operating in the system. This is clearly the case for Eu^{3+} complexes studied here because of unusually low luminescence intensities. For $\boldsymbol{YbL}^{3-5}$ and $\boldsymbol{YbL}^{3-5}_{\boldsymbol{NH2}}$, $q=0$ was found, in accordance with the solid-state structure. Overall, photophysical data show the successful sensitization of Eu^{3+} and Yb^{3+} luminescence by the chromophoric ligand, with a remarkable redshift of the absorption band for both $\boldsymbol{LnL}^{3}_{\boldsymbol{NH2}}$ vs. $\boldsymbol{LnL}^{3}$ and $\boldsymbol{LnL}^{5}_{\boldsymbol{NH2}}$vs. $\boldsymbol{LnL}^{5}$ pairs. This implies that upon the conjugation of enzyme-cleavable substrates to $\mathbf{L}^{3}$ and $\mathbf{L}^{5}$, the $\mathbf{EuL}^{3,5}$ and $\mathbf{YbL}^{3,5}$ complexes will behave as responsive optical imaging probes, with detection in the visible and the NIR regions, respectively. In the case of Yb^{3+} complexes, when going from $\mathbf{LnL}^{3}$ to $\mathbf{LnL}^{3}_{\mathbf{NH2}}$ or from $\mathbf{LnL}^{5}$ to $\mathbf{LnL}^{5}_{\mathbf{NH2}}$, emission intensity is enhanced by 42 and 18 times, respectively (Figure 2g, i), while for Eu^{3+} analogues it decreases in both cases by 3.5-fold (Figure S127g, i). Therefore, Yb^{3+} complexes are more preferable for the design of responsive optical imaging probes since they provide OFF-ON response, contrary to ON-OFF response for Eu^{3+}. The short excitation wavelength represents a limitation of these systems. We[49–50] and others[51–52] have previously shown that, however, substituents on the pyridine ring can lead to a significant redshift of the excitation wavelength. Such modifications are compatible with our molecular design and can be later implemented for the next-generation of imaging agents.

Relaxivity properties have been assessed for the Gd^{3+} chelates. Longitudinal water proton relaxivities, r_1, are 3.45, 3.80 and 3.96 $mM^{-1}s^{-1}$ for $\boldsymbol{GdL}^{n}$, and 2.58, 2.85 and 2.93 $mM^{-1}s^{-1}$ for the corresponding $\boldsymbol{GdL}^{n}_{\boldsymbol{NH2}}$ analogues ($n=3$, 4 and 5 respectively; 20 MHz, 37 °C, in water, Table S23), consistent with small, monohydrated Gd^{3+} complexes.[53] Since neither the carbamate nor the amine are in coordinating positions for the Ln^{3+} (see above, Figure 1), the hydration number does not vary between $\boldsymbol{GdL}^{n}$ and $\boldsymbol{GdL}^{n}_{\boldsymbol{NH2}}$. The 20–25 % decrease in relaxivities observed for $\boldsymbol{GdL}^{n}$ compared to $\boldsymbol{GdL}^{n}_{\boldsymbol{NH2}}$ can be thus attributed to a change of the rotational correlation time, τ_R, due to the decreased molecular weight. This was quantified for $\boldsymbol{GdL}^{5}$ ($\tau_R^{298}=94\pm3$ ps) and $\boldsymbol{GdL}^{5}_{\boldsymbol{NH2}}$ ($\tau_R^{298}=60\pm5$ ps) by analyzing the variable temperature ^1H Nuclear Magnetic Relaxation Dispersion profiles (Figure S134, Table S24). Therefore, we expect a more sizable relaxivity change for the enzyme-responsive agent bearing a larger leaving group.

ParaCEST spectra, plotted as normalized water signal intensity (M_z/M_0 %) against frequency offset (ppm), were recorded at variable pH for $\boldsymbol{LnL}^{3-5}$ and $\boldsymbol{LnL}^{3-5}_{\boldsymbol{NH2}}$ complexes (Ln^{3+} = Eu, Yb, 298 K, 3 s selective saturation at 25 μT, 0.5 ppm increments between −150 to +150 ppm; Figures S128–133). Independently of the pH (6.0–8.0), no CEST effect was observed for any of the Eu^{3+} complexes, nor for $\boldsymbol{YbL}^{3}$, $\boldsymbol{YbL}^{3}_{\boldsymbol{NH2}}$ and $\boldsymbol{YbL}^{4}_{\boldsymbol{NH2}}$. For $\boldsymbol{YbL}^{4}$, a weak effect appears as a shoulder of the bulk water signal. In contrast, two reasonable CEST effects are observed for $\boldsymbol{YbL}^{5}$ (13 ppm (13 %) and 24 ppm (6 %); pH 7.6) and $\boldsymbol{YbL}^{5}_{\boldsymbol{NH2}}$ (7 ppm (9 %) and 16 ppm (6 %); pH 7.5; Figure 3a, b). These are assigned to carbamate and amine protons, respectively, in the two diastereomeric (SAP and TSAP) forms of each complex,

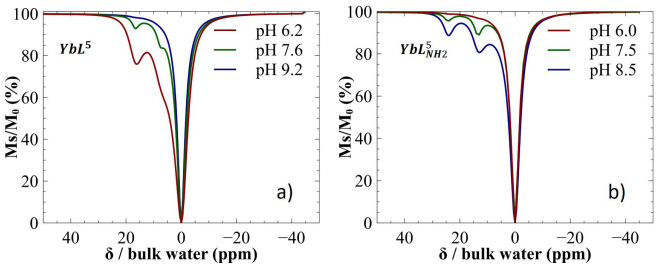

Figure 3. pH-dependent CEST spectra of 15.9 mM and 18.3 mM solutions of $\boldsymbol{YbL}^{5}$ (a) and $\boldsymbol{YbL}^{5}_{\boldsymbol{NH2}}$ (b), respectively (400 MHz, 25 μT saturation power during 3 s, H_2O/D_2O).

similarly to what was observed for $\boldsymbol{TbL}^{6}$,[25] and other Ln^{3+} complexes with exchangeable amide[54] or alcohol[55] protons.

SAP and TSAP diastereomers are detectable in the ^1H NMR spectra of all $\boldsymbol{EuL}^{n}$, $\boldsymbol{EuL}^{n}_{\boldsymbol{NH2}}$, $\boldsymbol{YbL}^{n}$ and $\boldsymbol{YbL}^{n}_{\boldsymbol{NH2}}$ complexes (Figures S53–65, Tables S1, S2). The lanthanide-induced shifts (LIS) of ligand protons depend on their relative position in respect to the Ln^{3+} (distance and orientation) and are higher for the SAP isomer.[56] SAP/TSAP ratios (1/0.4 and 1/0.8 for $\boldsymbol{YbL}^{5}$and $\boldsymbol{YbL}^{5}_{\boldsymbol{NH2}}$; 300 K) are slightly sensitive to temperature but not to pH (Figures S67–74, Table S3). The exchangeable carbamate protons of the two $\boldsymbol{YbL}^{5}$ isomers are also detectable in the ^1H NMR spectrum (Figure S74).

The molecular structures (see above, Figure 1) were used to rationalize the CEST observations. The lower CEST resonance frequency for $\boldsymbol{YbL}^{4}$ *vs.* $\boldsymbol{YbL}^{5}$ is the consequence of the longer carbamate H–Yb^{3+} distance (7.04 *vs* 5.65 Å, Table S16, Figure 1). The latter is similar for $\boldsymbol{YbL}^{3}$ (5.73 Å), but the angle (θ) describing the position of the carbamate H relatively to the axis passing through the macrocycle centroid and Yb^{3+} is significantly superior for $\boldsymbol{YbL}^{3}$ compared to $\boldsymbol{YbL}^{5}$ (69.83° vs. 24.51°, Table S16, Figure 1), resulting in lower LIS of the carbamate proton.[57] Due to the steric hindrance, the carbamate bond of $\boldsymbol{YbL}^{3}$ is not coplanar with the pyridine ring (Figure S122) preventing their tight electronic coupling and affecting the carbamate acidity, with consequences on the proton exchange rate, k_{ex}. CEST effects generated by $\boldsymbol{YbL}^{5}$ and $\boldsymbol{YbL}^{5}_{\boldsymbol{NH2}}$ are strongly pH sensitive (Figure 3), in accordance with the base- or acid-catalyzed exchange of carbamate[40] or amine[58–60] protons, respectively. This result is further demonstrated by the pH-dependence of k_{ex} that exhibits opposite trends for $\boldsymbol{YbL}^{5}$ and $\boldsymbol{YbL}^{5}_{\boldsymbol{NH2}}$ (Table S22). Despite the relatively small magnitude of these CEST effects, the opposite pH-dependence for the carbamate *vs.* the amine derivatives is appealing for the design of an enzyme-responsive $\boldsymbol{YbL}^{5}$ analogue, as it may increase the difference between the two forms at a given pH and/or allow for the detection of enzyme activity at different pHs.

Taken together, results of luminescence, relaxometric and CEST analysis suggest that the pyridine substitution in position 5 is the most promising for the design of enzyme-responsive probes. The carbamate $\boldsymbol{LnL}^{5}$, and the amine $\boldsymbol{LnL}^{5}_{\boldsymbol{NH2}}$ complexes, which mimic the "inactivated" and "activated" forms of an enzyme responsive multimodal

probe, can be distinguished by their T1 (Gd^{3+}) or paraCEST (Yb^{3+}) MRI as well as by their NIR optical properties (Yb^{3+}). Therefore, this system was selected for further development.

Enzyme responsive compounds

$\boldsymbol{LnL^5_{Gal}}$ analogues bearing a benzyl carbamate substituted by a β-galactoside have been prepared for the detection of β-galactosidase activity. The cleavage of the glycosidic bond by β-galactosidase triggers a self-immolative process that leads to the release of the corresponding $\boldsymbol{LnL^5_{NH2}}$ (Scheme 1), as it was indeed evidenced by LC–MS analysis for $\boldsymbol{YbL^5_{Gal}}$ (Figure S110). Apparent Michaelis–Menten kinetic parameters of the enzymatic cleavage, assessed by UV/Vis spectrophotometry, showed enhanced enzyme efficiency at pH = 6.2 vs. pH = 7.5 (Table S27).

As the next step, the enzymatic cleavage has been monitored by NIR luminescence and CEST for $\boldsymbol{YbL^5_{Gal}}$ and by relaxivity measurements for $\boldsymbol{GdL^5_{Gal}}$ (in 50 mM phosphate buffer containing 7.0 mg/mL BSA, at 310 K).

Excitation and absorption spectra of $\boldsymbol{YbL^5_{Gal}}$ resemble each other, and the characteristic Yb^{3+} NIR emission signal is observed upon excitation at 290 nm (Figure S148). The absorption spectrum of $\boldsymbol{YbL^5_{Gal}}$ is identical to that of $\boldsymbol{YbL^5}$; the $\boldsymbol{Q^L_{Yb}}$ values are similar (0.049 *vs.* 0.041 %), while τ_{obs} is longer for $\boldsymbol{YbL^5_{Gal}}$ (2.56 *vs.* 0.9 µs). The redshift (18 nm) of the maximum of the lower energy absorption band for $\boldsymbol{YbL^5_{NH2}}$ vs. $\boldsymbol{YbL^5_{Gal}}$ allows the monitoring of the enzymatic conversion by recording the pyridine-mediated NIR luminescence signal of Yb^{3+}. Indeed, enzymatic cleavage induces a time-dependent redshift of the excitation maxima upon monitoring the Yb^{3+} emission (Figure 4a) and a luminescence intensity increase at 978 nm (λ_{ex} = 320 nm; Figure 4b, c). Emission spectra are identical for $\boldsymbol{YbL^5_{Gal}}$ before and after the enzymatic cleavage, while the maximum of the excitation spectrum is shifted from 292 nm to 305 nm (Figure S148). The value of τ_{obs} remains the same within experimental error (2.25 vs. 2.56 µs), and $\boldsymbol{Q^L_{Yb}}$ increases 5.5-fold for $\boldsymbol{YbL^5_{Gal}}$ after the enzymatic cleavage (to 0.27 ± 0.01 %). The rate constant of the enzymatic cleavage was calculated from a monoexponential fit of the Yb^{3+} emission values as a function of the incubation time: $k_{obs} = 1.03\times10^{-3}\ s^{-1}$ ($t_{1/2}$ = 671 s), corresponding to a rate of $(1.86\pm0.12)\times10^{-5}$ µmol·s^{-1}·U^{-1} (0.2 mM $\boldsymbol{YbL^5_{Gal}}$, 0.8 U β-galactosidase; Figure 4c).

In CEST, as observed for the model compound $\boldsymbol{YbL^5}$, $\boldsymbol{YbL^5_{Gal}}$ has two carbamate-related effects which are stronger at pH 7.5 than at pH 6.0 (13, 24 ppm; Figure 5a–b). Upon incubation of $\boldsymbol{YbL^5_{Gal}}$ with β-galactosidase, these CEST peaks disappear in favor of two new ones at 9 ppm and 16 ppm attributed to the amine protons.

The time-dependent variation of normalized M_z/M_0 values was followed *via* selective saturation on the resonance frequencies of carbamate (13 and 24 ppm; pH 7.5) or amine protons (16 ppm; pH 6.2) to yield rate constants of $k_{obs}^{13ppm} = 6.22\times10^{-4}\ s^{-1}$ ($t_{1/2}$ = 1114 s), $k_{obs}^{24ppm} = 1.20\times10^{-3}\ s^{-1}$ ($t_{1/2}$ = 580 s) and $k_{obs}^{16ppm} = 2.38\times10^{-4}\ s^{-1}$ ($t_{1/2}$ = 2910 s), corresponding to rates of $(2.99\pm1.78)\times10^{-4}$ µmol.s^{-1}.U^{-1}, $(5.75\pm0.78)\times10^{-4}$ µmol.s^{-1}.U^{-1} and $(1.15\pm0.21)\times10^{-4}$ µmol.s^{-1}.U^{-1}, respectively (20 mM $\boldsymbol{YbL^5_{Gal}}$, 15 U β-galactosidase; Figure 5c–e). The slightly different rates measured at 13 and 24 ppm can be likely explained by the different concentration of SAP and TSAP isomers. Finally, similar rate constant, $k_{obs} = 3.27\times10^{-3}\ s^{-1}$ ($t_{1/2}$ = 212 s), corresponding to a rate of $(2.95\pm0.002)\times10^{-4}$ µmol.s^{-1}.U^{-1}, was calculated for the enzymatic transformation of $\boldsymbol{GdL^5_{Gal}}$, followed by the decrease of the relaxivity over time after adding β-galactosidase to the solution (1.5 mM $\boldsymbol{GdL^5_{Gal}}$; 6 U β-galactosidase, Figure 5f). Overall, these data evidence that the enzymatic conversion of $\boldsymbol{LnL^5_{Gal}}$ complexes occurs with a reasonably fast kinetics and can be followed *via* NIR luminescence, CEST or relaxivity changes.

Phantom imaging of the enzymatic reaction in optical imaging and MRI

In order to further demonstrate the capability of our system to image β-galactosidase activity with the complementary optical and MRI modalities, the enzymatic reaction has been monitored in aqueous solutions of the enzyme responsive probes by NIR optical ($\boldsymbol{YbL^5_{Gal}}$), and CEST ($\boldsymbol{YbL^5_{Gal}}$) or T1 ($\boldsymbol{GdL^5_{Gal}}$) MR imaging. The NIR luminescence was observed with a custom-designed NIR imaging

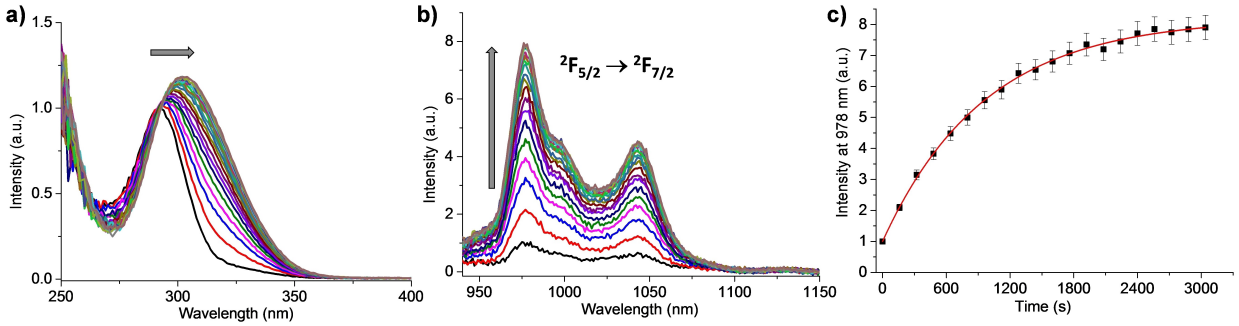

Figure 4. Time evolution of (a) excitation (λ_{em} = 978 nm) and (b) emission (λ_{ex} = 320 nm) spectra of 0.2 mM solution of $\boldsymbol{YbL^5_{Gal}}$ after addition of 0.8 U β-galactosidase (50 mM phosphate buffer with 7 mg/mL of BSA, pH = 7, room temperature). (c) Corresponding changes of Yb^{3+} emission intensity at 978 nm (black dots) and monoexponential fitting (red trace).

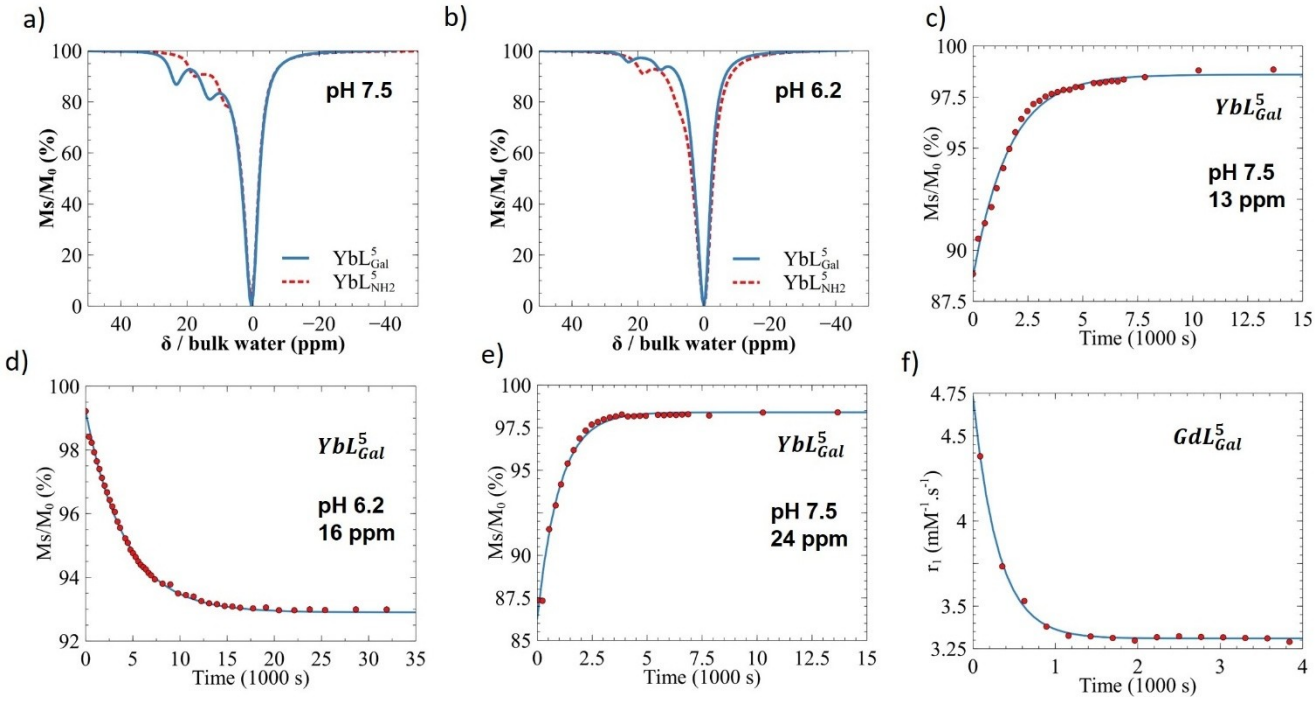

Figure 5. CEST spectra of $\boldsymbol{YbL^5_{Gal}}$ before (blue line) and after enzymatic reaction (red dashed line) at a) pH 7.5 and b) pH 6.2 (3 s selective saturation at 25 μT, 0.5 ppm increments, 400 MHz). Time-dependent magnetization in 20 mM $\boldsymbol{YbL^5_{Gal}}$ (15 U β-galactosidase, 0.5 mL) at c) pH 7.5, 13 ppm; d) pH 7.5, 24 ppm; e) pH 6.2, 16 ppm. f) Time-dependent relaxivity changes in 1.5 mM $\boldsymbol{GdL^5_{Gal}}$ (6 U β-galactosidase, 0.5 mL, 20 MHz, pH 7.5). 37 °C, 50 mM phosphate, 7.0 mg/mL BSA.

system in a 2 mM solution of $\boldsymbol{YbL^5_{Gal}}$ after addition of 8 U *β*-galactosidase, upon excitation at 320 nm. Collected images show the increase of the NIR intensity over time, in accordance with the formation of $\boldsymbol{YbL^5_{NH2}}$, having selective absorption at this wavelength (Figure 6a, Table S29). No change was observed in control samples (buffer and $\boldsymbol{YbL^5_{Gal}}$ without enzyme). Such NIR imaging demonstration of the applicability of our system is remarkable and unique in the

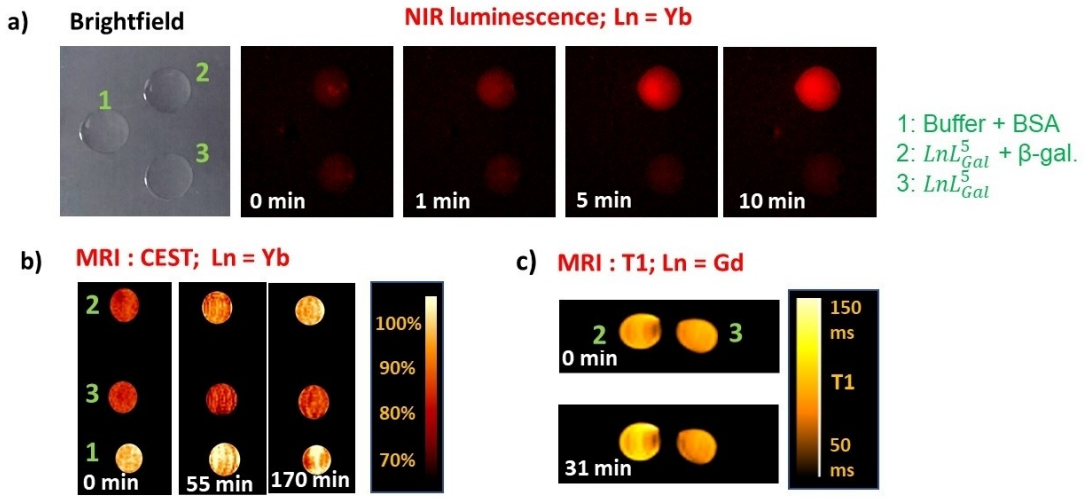

Figure 6. a) Brightfield and NIR luminescence images (λ_{ex} = 320 nm; λ_{em} = 996 nm band pass 70 nm filter; τ_{exp} = 10 ms, 310 K). (1) reference: 50 mM phosphate buffer, 7 mg/mL BSA, pH 7.5; (2) reference + 2 mM $\boldsymbol{YbL^5_{Gal}}$ + 8 U β-galactosidase; (3) reference + 2 mM YbL^5_{Gal}. b) CEST images acquired using a spin-echo sequence; TR/TE = 5000 ms/11.8 ms, with 25μT and 4 s presaturation pulse, B = 9.4T. (1) reference: 100 mM phosphate buffer, 7 mg/mL BSA, pH 7.4; (2) reference + 13.9 mM $\boldsymbol{YbL^5_{Gal}}$ + 5 U β-galactosidase; (3) reference + 13.9 mM $\boldsymbol{YbL^5_{Gal}}$.c) T1 maps acquired using a spin-echo sequence; TE = 8.2 ms; TR = 15–1000 ms, 9.4 T. (2) 1.7 mM $\boldsymbol{GdL^5_{Gal}}$; 3.1 U β-galactosidase; 100 mM phosphate buffer, 7 mg/mL BSA, pH 7.5. (3) 1.7 mM $\boldsymbol{GdL^5_{Gal}}$; 100 mM phosphate buffer, 7 mg/mL BSA, pH 7.5. T = 310 K.

literature. Indeed, previous reports on Ln^{3+}-based enzyme detection using luminescence imaging relied exclusively on visible-emitting ions.[10,13,61–64]

CEST MRI phantom images have been acquired on a 9.4 T imaging spectrometer for a 13.9 mM $\boldsymbol{YbL^5_{Gal}}$ solution after addition of 5 U β-galactosidase, with a selective saturation at 23 ppm corresponding to the carbamate proton resonance (Figure 6b, Table S30). The CEST effect, decreasing over time, originates from the disappearance of the carbamate proton due to the enzymatic cleavage. Finally, T1-weighted MR images recorded on a 1.7 mM $\boldsymbol{GdL^5_{Gal}}$ solution in the presence of 3.1 U β-galactosidase also show an intensity change resulting from the transformation of the probe (Figure 6c, Table S31). To the best of our knowledge, this is the first example where a single ligand, complexed to Ln^{3+} of different natures is used to image an enzymatic activity in optical, as well as CEST and T1-MR imaging modalities.

Conclusion

The visualization of active enzymes in several complementary imaging techniques is of primary importance, and in such applications, the use of a single probe that generates a specific signal in all those modalities is highly desired. With this goal in mind, we have designed Ln^{3+} complexes that can provide detectable, enzyme-mediated changes in NIR luminescence, as well as in CEST and T1 MRI, depending on the nature of the Ln^{3+} used. A comprehensive structural, photophysical and NMR analysis in a family of carbamate- and amine-derivatives of these Ln^{3+}-DO3A-pyridine model chelates allowed us to rationalize the respective imaging properties as a function of the molecular structure, and to select the ligand possessing the most promising properties for the design of a β-galactosidase-responsive probe, $\boldsymbol{LnL^5_{Gal}}$. We have shown that $\boldsymbol{LnL^5_{Gal}}$ undergoes enzymatic cleavage with a reasonably fast kinetics, and the system retains sufficient NIR luminescence, CEST and relaxivity changes in the enzyme-mediated process. Most importantly, we have demonstrated the successful visualization of an enzyme activity using a unique ligand in NIR luminescence and CEST MRI imaging in phantoms containing $\boldsymbol{YbL^5_{Gal}}$ and in T1 MRI when using $\boldsymbol{GdL^5_{Gal}}$. A great advantage of this probe design is its high versatility, as there are a large number of enzymatically cleavable groups that could be attached to the $\boldsymbol{L^5}$ core,[65] thus creating probes for other important biological targets. We believe that these results demonstrate the strong potential of Ln^{3+} complexes for multimodal responsive imaging.

Experimental Section

Experimental procedures are described in detail in the Supporting Information.

Supporting Information

Materials and methods, synthetic procedures, compounds characterization, NMR spectra of the intermediates and of the complexes, assignment and temperature dependencies of NMR spectra of the complexes, HPLC analyses, UPLC analysis of enzyme reaction, crystallographic details (ORTEP, Data collection and structure refinements) and discussion, photophysical procedures, CEST (spectra) and relaxivity measurements (NMRD), monitoring of enzyme kinetic by UV, NIR luminescence, relaxivity and PARACEST NMR, phantom imaging. Deposition Numbers 2182710 (for $\boldsymbol{YbL^3}$), 2223144 (for $\boldsymbol{YbL^4}$), 2045612 (for $\boldsymbol{YbL^5}$), 2223877 (for $\boldsymbol{YbL^3_{NH2}}$), 2211205 (for $\boldsymbol{YbL^4_{NH2}}$), and 2177885 (for $\boldsymbol{YbL^5_{NH2}}$) contain the supplementary crystallographic data for this paper. These data are provided free of charge by the joint Cambridge Crystallographic Data Centre and Fachinformationszentrum Karlsruhe Access Structures service at http://www.ccdc.cam.ac.uk/structures. The authors have cited additional references within the Supporting Information.[66–77]

Acknowledgements

The authors thank the French National Research Agency (grant ANR-2010-1513-01) and the Ligue contre le Cancer du Grand Ouest for funding. S.P. acknowledges support from Institut National de la Santé et de la Recherche Médicale (INSERM). Financial support from the Institute of Chemistry of Natural Substances (ICSN) for R. J. and J. M. is greatly acknowledged. We thank V. Steinmetz and N. Hue from the analytical platform of ICSN for the HPLC analyses and the MO2VING platform of CBM for the MRI, MS and NMR facilities.

Conflict of Interest

The authors declare no conflict of interest.

Data Availability Statement

The data that support the findings of this study are available in the supplementary material of this article.

Keywords: multimodal imaging · enzymatic detection · NIR luminescence · lanthanide · MRI

[1] T. D. Meek, in *Burger's Medicinal Chemistry and Drug Discovery* (Ed.: D. J. Abraham), **2023**, pp. 1–51.
[2] C. J. Yang, Q. Wang, W. Ding, *RSC Adv.* **2019**, *9*, 25285–25302.
[3] D. V. Hingorani, B. Yoo, A. S. Bernstein, M. D. Pagel, *Chem. Eur. J.* **2014**, *20*, 9840–9850.
[4] A. A. Gilad, A. Bar-Shir, A. R. Bricco, Z. Mohanta, M. T. McMahon, *NMR Biomed.* **2023**, *36*,e4712.

[5] H. Q. Han, Y. F. Zhong, C. He, L. Fu, Q. T. Huang, Y. Kuang, X. Q. Yi, W. J. Zeng, H. F. Zhong, M. Yang, *Dyes Pigm.* **2022**, *204*, 110386

[6] Y. Q. Wang, J. H. Weng, X. D. Wen, Y. X. Hu, D. J. Ye, *Biomat. Sci.* **2021**, *9*, 406–421.

[7] Y. Wang, Y. X. Hu, D. J. Ye, *Angew. Chem. Int. Ed.* **2022**, *61*, e202209512.

[8] M. L. James, S. S. Gambhir, *Physiol. Rev.* **2012**, *92*, 897–965.

[9] A. Y. Louie, *Chem. Rev.* **2010**, *110*, 3146–3195.

[10] E. Pershagen, K. E. Borbas, *Angew. Chem. Int. Ed.* **2015**, *54*, 1787–1790.

[11] J. Meyer, U. Karst, *Analyst* **2000**, *125*, 1537–1538.

[12] T. Terai, H. Ito, K. Hanaoka, T. Komatsu, T. Ueno, T. Nagano, Y. Urano, *Bioorg. Med. Chem. Lett.* **2016**, *26*, 2314–2317.

[13] S. H. Hewitt, S. J. Butler, *Chem. Commun.* **2018**, *54*, 6635–6647.

[14] A. Merbach, L. Helm, E. Toth, *The Chemistry of Contrast Agents in Medical Magnetic resonance Imaging*, Second Edition ed., John Wiley & Sons, Chichester, **2013**.

[15] J. Wahsner, E. M. Gale, A. Rodríguez-Rodríguez, P. Caravan, *Chem. Rev.* **2018**, 957-1057

[16] H. Dafni, A. Gilead, N. Nevo, R. Eilam, A. Harmelin, M. Neeman, *Magn. Reson. Med.* **2003**, *50*, 904–914.

[17] M. M. Huber, A. B. Staubli, K. Kustedjo, M. H. B. Gray, J. Shih, S. E. Fraser, R. E. Jacobs, T. J. Meade, *Bioconjugate Chem.* **1998**, *9*, 242–249.

[18] C. Rivas, G. J. Stasiuk, J. Gallo, F. Minuzzi, G. A. Rutter, N. J. Long, *Inorg. Chem.* **2013**, *52*, 14284–14293.

[19] V. S. R. Harrison, C. E. Carney, K. W. MacRenaris, E. A. Waters, T. J. Meade, *J. Am. Chem. Soc.* **2015**, *137*, 9108–9116.

[20] E. Debroye, T. N. Parac-Vogt, *Chem. Soc. Rev.* **2014**, *43*, 8178–8192.

[21] A. Keliris, T. Ziegler, R. Mishra, R. Pohmann, M. G. Sauer, K. Ugurbil, J. Engelmann, *Bioorg. Med. Chem.* **2011**, *19*, 2529–2540.

[22] R. Q. Yan, Y. X. Hu, F. Liu, S. X. Wei, D. Q. Fang, A. J. Shuhendler, H. Liu, H. Y. Chen, D. J. Ye, *J. Am. Chem. Soc.* **2019**, *141*, 10331–10341.

[23] H. Li, G. Parigi, C. Luchinat, T. J. Meade, *J. Am. Chem. Soc.* **2019**, *141*, 6224–6233.

[24] M. Suchy, R. Ta, A. X. Li, F. Wojciechowski, S. H. Pasternak, R. Bartha, R. H. E. Hudson, *Org. Biomol. Chem.* **2010**, *8*, 2560–2566.

[25] J. F. He, C. S. Bonnet, S. V. Eliseeva, S. Lacerda, T. Chauvin, P. Retailleau, F. Szeremeta, B. Badet, S. Petoud, E. Toth, P. Durand, *J. Am. Chem. Soc.* **2016**, *138*, 2913–2916.

[26] T. Chauvin, P. Durand, M. Bernier, H. Meudal, B. T. Doan, F. Noury, B. Badet, J. C. Beloeil, E. Toth, *Angew. Chem. Int. Ed.* **2008**, *47*, 4370–4372.

[27] J. A. Duimstra, F. J. Femia, T. J. Meade, *J. Am. Chem. Soc.* **2005**, *127*, 12847–12855.

[28] L. M. Lilley, S. Kamper, M. Caldwell, Z. K. Chia, D. Ballweg, L. Vistain, J. Krimmel, T. A. Mills, K. MacRenaris, P. Lee, E. A. Waters, T. J. Meade, *Angew. Chem. Int. Ed.* **2020**, *59*, 388–394.

[29] R. C. Wang, X. Z. Wang, X. F. Gu, Y. C. Liu, C. C. Zhao, *Sens. Actuators B* **2023**, *380*, 133282.

[30] J. H. Tang, H. Li, C. N. Yuan, G. Parigi, C. Luchinat, T. J. Meade, *J. Am. Chem. Soc.* **2023**, *145*, 10045–10050.

[31] L. M. Lilley, S. Kamper, M. Caldwell, Z. K. Chia, D. Ballweg, L. Vistain, J. Krimmel, T. A. Mills, K. MacRenaris, P. Lee, E. A. Waters, T. J. Meade, *Angew. Chem. Int. Ed.* **2020**, *59*, 388–394.

[32] Y. Valieva, E. Ivanova, A. Fayzullin, A. Kurkov, A. Igrunkova, *Diagnostik* **2022**, *12*, 2309.

[33] H. W. Liu, L. L. Chen, C. Y. Xu, Z. Li, H. Y. Zhang, X. B. Zhang, W. H. Tan, *Chem. Soc. Rev.* **2018**, *47*, 7140–7180.

[34] C. Geraldes, J. A. Peters, *Molecules* **2022**, *27*, 8297.

[35] Y. K. Yao, Y. T. Zhang, C. X. Yan, W. H. Zhu, Z. Q. Guo, *Chem. Sci.* **2021**, *12*, 9885–9894.

[36] H. Singh, K. Tiwari, R. Tiwari, S. K. Pramanik, A. Das, *Chem. Rev.* **2019**, *119*, 11718–11760.

[37] J. J. Zhang, P. H. Cheng, K. Y. Pu, *Bioconjugate Chem.* **2019**, *30*, 2089–2101.

[38] S. K. Sharma, S. P. Sharma, R. M. Leblanc, *Enzyme Microb. Technol.* **2021**, *150*, 109885.

[39] M. Wyskocka-Gajda, L. Przypis, M. Olesiejuk, T. Krawczyk, A. Kuznik, K. Nawara, M. Minoshima, F. Sugihara, K. Kikuchi, N. Kuznik, *Eur. J. Med. Chem.* **2021**, *211*, 113086.

[40] R. Pollet, C. S. Bonnet, P. Retailleau, P. Durand, E. Toth, *Inorg. Chem.* **2017**, *56*, 4317–4323.

[41] I. Lukeš, J. Kotek, P. Vojtíšek, P. Hermann, *Coord. Chem. Rev.* **2001**, *216–217*, 287–312.

[42] A. Spek, *Acta Crystallogr. Sect. D* **2009**, *65*, 148–155.

[43] C. F. Macrae, P. R. Edgington, P. McCabe, E. Pidcock, G. P. Shields, R. Taylor, M. Towler, J. van de Streek, *J. Appl. Crystallogr.* **2006**, *39*, 453–457.

[44] A. G. Cosby, J. J. Woods, P. Nawrocki, T. J. Sørensen, J. J. Wilson, E. Boros, *Chem. Sci.* **2021**, *12*, 9442–9451.

[45] D. Kovacs, E. Mathieu, S. R. Kiraev, J. A. L. Wells, E. Demeyere, A. Sipos, K. E. Borbas, *J. Am. Chem. Soc.* **2020**, *142*, 13190–13200.

[46] D. Kocsi, D. Kovacs, J. A. L. Wells, K. E. Borbas, *Dalton Trans.* **2021**, *50*, 16670–16677.

[47] R. M. Supkowski, W. D. Horrocks, *Inorg. Chim. Acta* **2002**, *340*, 44–48.

[48] A. Beeby, I. M. Clarkson, R. S. Dickins, S. Faulkner, D. Parker, L. Royle, A. S. de Sousa, J. A. G. Williams, M. Woods, *J. Chem. Soc. Perkin Trans. 2* **1999**, 493–503.

[49] C. S. Bonnet, F. Buron, F. Caille, C. M. Shade, B. Drahos, L. Pellegatti, J. Zhang, S. Villette, L. Helm, C. Pichon, F. Suzenet, S. Petoud, É. Tóth, *Chem. Eur. J.* **2012**, *18*, 1419–1431.

[50] F. Caille, C. S. Bonnet, F. Buron, S. Villette, L. Helm, S. Petoud, F. Suzenet, E. Toth, *Inorg. Chem.* **2012**, *51*, 2522–2532.

[51] E. R. H. Walter, J. A. G. Williams, D. Parker, *Chem. Eur. J.* **2018**, *24*, 7724–7733.

[52] M. Starck, R. Pal, D. Parker, *Chem. Eur. J.* **2016**, *22*, 570–580.

[53] S. Laurent, L. V. Elst, R. N. Muller, *Contrast Media Mol. Imaging* **2006**, *1*, 128–137.

[54] T. K. Stevens, M. Milne, A. A. H. Elmehriki, M. Suchy, R. Bartha, R. H. E. Hudson, *Contrast Media Mol. Imaging* **2013**, *8*, 289–292.

[55] D. Delli Castelli, E. Terreno, S. Aime, *Angew. Chem. Int. Ed.* **2011**, *50*, 1798–1800.

[56] S. Viswanathan, Z. Kovacs, K. N. Green, S. J. Ratnakar, A. D. Sherry, *Chem. Rev.* **2010**, *110*, 2960–3018.

[57] E. N. Zapolotsky, Y. Y. Qu, S. P. Babailov, *J. Inclusion Phenom. Macrocyclic Chem.* **2022**, *102*, 1–33.

[58] T. Chauvin, S. Torres, R. Rosseto, J. Kotek, B. Badet, P. Durand, E. Toth, *Chem. Eur. J.* **2012**, *18*, 1408–1418.

[59] G. S. Liu, Y. G. Li, M. D. Pagel, *Magn. Reson. Med.* **2007**, *58*, 1249–1256.

[60] P. B. Tsitovich, J. M. Cox, J. A. Spernyak, J. R. Morrow, *Inorg. Chem.* **2016**, *55*, 12001–12010.

[61] M. T. Gabr, A. Balupuri, N. S. Kang, *ACS Sens.* **2020**, *5*, 1872–1876.

[62] E. Pershagen, K. E. Borbas, *Coord. Chem. Rev.* **2014**, *273*, 30–46.

[63] E. M. Surender, S. J. Bradberry, S. A. Bright, C. P. McCoy, D. C. Williams, T. Gunnlaugsson, *J. Am. Chem. Soc.* **2017**, *139*, 381–388.

[64] J. W. Wang, Y. B. Jin, M. D. Li, S. J. Liu, K. K. W. Lo, Q. Zhao, *Chem. Asian J.* **2022**, *17*, e202200429.

[65] J. Yan, S. Lee, A. Zhang, J. Yoon, *Chem. Soc. Rev.* **2018**, *47*, 6900–6916.
[66] J. A. Peters, K. Djanashvili, C. F. G. C. Geraldes, C. Platas-Iglesias, in *The Chemistry of Contrast Agents in Medical Magnetic Resonance Imaging* (Eds.: A. Merbach, L. Helm, E. Toth), Wiley-VCH, **2013**, pp. 209–276.
[67] F. Benetollo, G. Bombieri, L. Calabi, S. Aime, M. Botta, *Inorg. Chem.* **2003**, *42*, 148–157.
[68] O. V. Dolomanov, L. J. Bourhis, R. J. Gildea, J. A. K. Howard, H. Puschmann, *J. Appl. Crystallogr.* **2009**, *42*, 339–341.
[69] M. Woods, S. Aime, M. Botta, J. A. K. Howard, J. M. Moloney, M. Navet, D. Parker, M. Port, O. Rousseaux, *J. Am. Chem. Soc.* **2000**, *122*, 9781–9792.
[70] S. Aime, M. Botta, G. Ermondi, *Inorg. Chem.* **1992**, *31*, 4291–4299.
[71] L. Di Bari, G. Pintacuda, P. Salvadori, R. S. Dickins, D. Parker, *J. Am. Chem. Soc.* **2000**, *122*, 9257–9264.
[72] T. Krchová, V. Herynek, A. Gálisová, J. Blahut, P. Hermann, J. Kotek, *Inorg. Chem.* **2017**, *56*, 2078–2091.
[73] A. Barge, G. Cravotto, E. Gianolio, F. Fedeli, *Contrast Media Mol. Imaging* **2006**, *1*, 184–188.
[74] M. Lovric, I. Cepanec, M. Litvic, A. Bartolincic, V. Vinkovic, *Croat. Chem. Acta* **2007**, *80*, 109–115.
[75] H. J. Schuster, B. Krewer, J. M. von Hof, K. Schmuck, I. Schuberth, F. Alves, L. F. Tietze, *Org. Biomol. Chem.* **2010**, *8*, 1833–1842.
[76] G. A. Molander, B. W. Katona, F. Machrouhi, *J. Org. Chem.* **2002**, *67*, 8416–8423.
[77] G. A. Molander, A. R. Brown, *J. Org. Chem.* **2006**, *71*, 9681–9686.

Manuscript received: November 21, 2023
Accepted manuscript online: February 20, 2024
Version of record online: March 12, 2024